CRYSTAL GROWTH & DESIGN

pubs.acs.org/crystal Article

Design of Novel Solid-State Electrolytes Based on Plastic Crystals of Quinuclidinolium Methanesulfonate for Proton Conduction

Samet Ocak, Federico Poli, Dario Braga, Tommaso Salzillo,* Fabrizio Tarterini, Gianluca Carì, Elisabetta Venuti, Francesca Soavi,* and Simone d'Agostino*

Cite This: https://doi.org/10.1021/acs.cgd.3c00145 Read Online

ABSTRACT: A series of methanesulfonate salts with various globular cations, including the achiral 3-quinuclidonium $[QHco]^+$, the racemic (3)-hydroxyquinuclidinium $[QHrac]^+$, and the enantiopure (3)-hydroxyquinuclidinium R-$[QH]^+$, have been synthesized and structurally characterized. Despite the high degree of similarity among components, only the enantiopure salt R-[QH]MS was found to undergo a reversible plastic transition at high temperature. Electrochemical impedance spectroscopy was successfully applied to study proton conductivity associated with temperature variations and the plastic phase transition under inert and dry conditions. Ionic conductivity at RT was lower than 10^{-11} S cm^{-1} and drastically increased up to 1.03×10^{-3} S cm^{-1} at 145 °C due to the onset of the plastic phase transition.

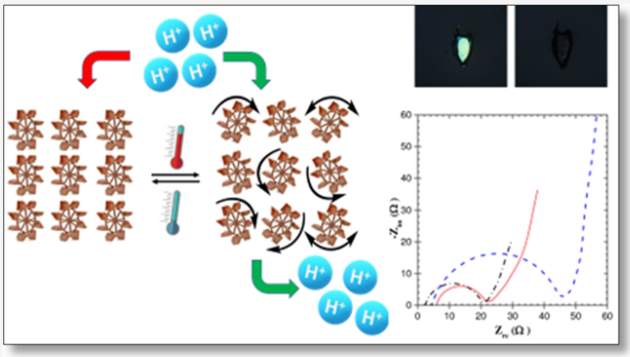

INTRODUCTION

The development of proton-conducting materials is at the forefront of current research efforts since they are key components in many electric devices, including sensors, supercapacitors, batteries, and fuel cells.[1−6] Although many researchers have been focusing on the development of various proton-conducting materials, Nafion membranes are today the most widely used.[7,8] However, there are still some drawbacks to their utilization since these materials suffer from high costs for large-scale production and strict operating conditions; e.g., Nafion shows high proton conductivity only in the hydrated form, whereas conductivity performances drastically drop due to dehydration processes at high temperatures (above ~80 °C).[9−12] Therefore, the development of cheap and easily processable proton conduction materials is mandatory to increase the working temperature of the devices to above 100 °C.

Recent efforts have identified ionic plastic crystals (IPCs) as promising candidates for the development of novel solid-state electrolytes or as dopants to be incorporated within Nafion-based membranes.[13−16] As electrolyte materials, they offer several advantages such as non-inflammability, low vapor pressure, plasticity, higher thermal stability, and of course, intrinsic ionic conductivity favored by their intrinsic dynamic nature.[13,17−25]

IPCs are materials characterized by long-range crystalline order, while their components feature reorientational processes in the solid state, such as molecular rotations or librations around their center of mass.[19,25−30] The typical approach in designing such materials relies on choosing suitable building blocks and controlling the potential mobile component's free volume in the local environment by applying suitable stimuli, e.g., temperature and pressure variations,[31−36] which may weaken the intermolecular interactions and lower the packing density,[32−35,37,38] leading to dynamically disordered phases. Therefore, globular molecular ions[13,39−44] and stimuli to achieve loosely packed structures are desirable to favor reorientation and hence increase the occurrence of plastic phases. Salts of bulky, disk-like, or planar cations like imidazolium,[45,46] metallocenium,[47,48] and quinuclidinium[49,50] derivatives are prone to exhibit plastic phases at high temperatures owing to their shapes. However, it is challenging to establish a priori which combination of ionic components would work or not as it is also challenging to predict the transition temperature at which molecular plastic phases form. Hence, the comprehension of the molecular and structural factors responsible for such transitions and the quest for new design methods for expanding and modulating the plastic phase transitions are at the cutting edge in this field.

In previous studies, we, and others, have reported the observation of plastic phase behaviors in molecular salts

Received: February 13, 2023
Revised: April 18, 2023

containing the enantiopure cation (3)-hydroxyquinuclidinium with various anions,[51−53] and by applying the principles of crystal engineering,[88,89] we have also explored the possibility of accessing solid solutions with different anions to permit fine control over the transition temperature.[28,35,54−56]

In this work, we aim at elucidating the effect of the crystal packing features on the plastic transition behaviors in a family of materials that are expected to afford ionic plastic phases as a function of temperature. In this way, we expect to highlight novel structural factors responsible for the occurrence or not of the plastic transition and achieve insights that can be further applied to the design principles of such materials.

To this end, we synthesized a series of methanesulfonate salts with various globular cations, including the achiral 3-quinuclidonium $[QHco]^+$, the racemic (3)-hydroxyquinuclidinium $[QHrac]^+$, and the enantiopure (3)-hydroxyquinuclidinium R-$[QH]^+$, see Chart 1; at the same time, the methanesulfonate anion (MS) was selected to mimic the sulfonic acid moiety of Nafion.

Chart 1. Molecular Structures of the Ions Chosen as Components for the Preparation of IPCs: (a) the Methanesulfonate Anion, (b) the Achiral 3-Quinuclidonium $[QHco]^+$, (c) the Racemic Hydroxyquinuclidinium $[QHrac]^+$, and (d) the Enantiopure R-Hydroxyquinuclidinium R-$[QH]^+$ Cations, * Indicates the Chiral Center

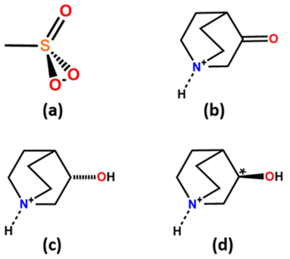

We deliberately chose this series of cations to investigate the plastic transition dependence on the chirality of the system and difference in hydrogen-bonding capacity. Achiral molecules/ions can crystallize in either chiral or achiral packings,[57] whereas racemic mixtures may take different routes and crystallize as true racemates (crystals containing equal amounts of right- and left-handed species) or separate out and form racemic conglomerates (physical mixtures of enantiomorphic crystals of the corresponding handedness).[58] On the other hand, chiral species are forced to crystallize into a chiral structure.[59] At the same time, hydrogen bond formation remains one of the major forces driving the crystallization of specific interaction patterns; therefore, both factors are expected to profoundly affect the intermolecular interaction patterns and crystal packings within this family of salts.

■ EXPERIMENTAL SECTION

Synthesis. All reagents and reactants were purchased from Sigma-Aldrich and used without any further purification. Bi-distilled water and reagent grade solvents were used.

The salts [QHco]MS, [QHrac]MS, and R-[QH]MS were obtained by the anion exchange reaction between the halide abstraction reagent, silver methanesulfonate ($AgSO_3CH_3$), and the corresponding hydrochloride salts of the quinuclidinium derivative. In a typical reaction, 100 mg (0.5 mmol) of $AgSO_3CH_3$ was dissolved in a beaker with 3 mL of water and left under stirring at RT. Next, the stoichiometric amount of hydrochloride salts of the quinuclidinium derivative was dissolved in another beaker with ca. 2 mL of water. The resulting solution was added dropwise to the solution of $AgSO_3CH_3$ and left under stirring for ca. 2 h. Then, the precipitated AgCl was filtered off, and the resulting solution was left to slowly evaporate to afford viscous liquids. Crystallization was achieved by keeping the resulting liquids at 60 °C (oven) for ca. 72 h. Only for R-[QH]MS, good crystals suitable for single-crystal analysis were achieved, while [QHco]MS and [QHrac]MS afforded crystalline materials as flakes which were analyzed through powder XRD (vide infra).

X-ray Diffraction (XRD). Single-crystal data for R-[QH]MS was collected on an Oxford X'Calibur S CCD diffractometer fitted with a graphite monochromator (Mo-Kα radiation). The structure was solved with SHELXT[62] by intrinsic phasing and refined on F^2 with SHELXL[63] implemented in the $Olex^2$ software[64] by full-matrix least squares refinement. All non-hydrogen atoms were anisotropically refined and the rigid-body RIGU restraints applied.[65] H_{OH} and H_{NH} atoms were directly located, when possible, while H_{CH} atoms were added in calculated positions and refined riding on their respective carbon atoms. Data collection and refinement details are listed in Table S1. The Mercury[66] program was used for molecular graphics and calculation of intermolecular interactions. For phase identification and variable-temperature X-ray powder diffraction purposes, measurements were performed on a PANalytical X'Pert Pro automated diffractometer equipped with an X'Celerator detector in Bragg−Brentano geometry, using Cu−Kα radiation without a monochromator in the 2θ range between 5 and 40° (continuous scan mode, step size 0.0167°, counting time 19.685 s, Soller slit 0.04 rad, antiscatter slit 1/2, divergence slit 1/4, 40 mA × 40 kV) and with an Anton-Paar TTK 450 + LNC. The program Mercury[66] was used for the calculation of powder XRD patterns based on single-crystal data collected in this work. Chemical and structural identities between bulk materials and single crystals were always verified by comparing experimental and calculated powder diffraction patterns (Figure S1). For the structural solution of [QHco]MS and [QHrac]MS, diffractograms in the 2θ range 3−70° (step size, 0.026°; time/step, 200 s; 0.02 rad soller; $V \times A$ 40 × 40) were collected on a Panalytical X'Pert PRO automated diffractometer equipped with a PIXcel detector in transmission geometry (capillary spinner), using Cu−Kα radiation without a monochromator in the 2θ range 3−70° (continuous scan mode, step size 0.0260°, counting time 889.70 s, Soller slit 0.02, antiscatter slit 1/4, divergence slit 1/4, 40 mA × 40 kV). Five diffraction patterns were recorded and summed to enhance the signal-to-noise ratio. Powder diffraction data were analyzed with the software EXPO2014,[67] which is designed to analyze both monochromatic and non-monochromatic data. Selected peaks were chosen in the 2θ range 10−50°, and unit cell constants were found using the algorithm N-TREOR09.[68] Structures were solved by simulated annealing employing fragments retrieved from the CCDC[69] and refined as a rigid body with the software EXPO2014.[67] An overall thermal parameter for all the atoms was adopted. See Figures S2 and S3 for the pattern difference plots and Table S1 for crystallographic details. Crystal data can be obtained free of charge via www.ccdc.cam.ac.uk/conts/retrieving.html (or from the Cambridge Crystallographic Data Centre, 12 Union Road, Cambridge CB21EZ, UK; fax: (+44)1223-336-033; or e-mail: deposit@ccdc.cam.ac.uk); CCDC numbers2235832−2235834.

Thermal Analyses. TGA was performed with a PerkinElmer TGA-7. The sample was contained in a platinum crucible and heated under nitrogen flow (20 cm^3 min^{-1}) at a rate of 5 K min^{-1} up to decomposition. Sample weight was in the range 5−10 mg. Calorimetric measurement was performed with a PerkinElmer DSC-7 equipped with a PII intracooler. Temperature and enthalpy calibrations were performed using high-purity standards (n-decane, benzene, and indium). Heating of the aluminum open pan containing the sample (3−5 mg) was carried out at 5 K min^{-1} in the temperature range 243−473 K under a N_2 atmosphere. Entropy change was estimated by dividing the enthalpy change by the transition temperature. Hot-stage experiment was carried out using a Linkam TMS94 device connected to a Linkam LTS350 platinum plate and equipped with polarizing filters. Images were collected with a NIKON DS FI3 camera from an Olympus BX41 stereomicroscope.

Raman Spectroscopy. Raman spectra were recorded with a Horiba T64000 triple spectrometer coupled to an Olympus BX41 microscope equipped with 100×, 50×, 20×, and 5× objectives. The spectrometer with a 640 mm focal length was equipped with a Peltier thermoelectric cooled CCD of 1024 × 256 pixels and a diffraction grating of 1800 grooves per mm. The Rayleigh scattering was removed working in a double subtractive combined with a single additive mode, thus allowing for the detection of a minimum Raman shift of approximately 5 cm^{-1}. The setup allowed for a spatial resolution below 1 μm with the 100× objective, a nominal field depth ranging from about 25 to 450 μm, and a spectral resolution down to 0.5 cm^{-1}. The excitation was from a Krypton ion gas laser tuned at 647.1 nm with a nominal power of 500 mW. In all the experiments, the power was reduced by neutral density filters to avoid sample damage. Variable-temperature measurements were carried out with a Linkam TMS94 device using the long distance of a 20× objective which guaranteed a working distance of 21 mm.

Electrochemical Impedance Spectroscopy. Ionic conductivity was measured by electrochemical impedance spectroscopy (EIS) on 13 mm diameter pellets, featuring a thickness of 0.75 mm, pressed at 10 tons for 5 min, and coated with silver paint. After the first heating and cooling cycle of the R-[QH]MS sample, we realized a decrease in the thickness to 0.5 mm and an increment in the cross-sectional area of the pellet which is an insurgence of the plastic phase change of this material. The conductivity values of the further cycles are calculated with new dimensions. To exclude any contribution from humidity to the sample ionic conductivity, before measurements, the pellets were dried at 80 °C under vacuum oven 12 h (Büchi glass oven B-585) and then transferred in a dry box (Ar atmosphere, H_2O, and $O_2 < 1$ ppm MBraun) for cell assembly and test. The pellets were placed between two stainless steel blocking electrodes (1.6 cm diameter) housed in a two-electrode, Swagelok-type cell. The EIS spectra were collected by a VSP multichannel potentiostat/galvanostat/FRA (BioLogic, Seyssinet-Pariset, France) within the 700 kHz−10 mHz frequency range and with an AC perturbation that was lowered from an initial value of 100 to 25 mV at increasing temperature to adjust the current density due to the impedance reduction, acquiring 5 points per decade. The cells were thermostated at different temperatures (from 25 to 145 °C) by a Büchi glass oven B-585 placed inside the dry box. Samples were thermostated for 30 min before every measurement. The EIS Nyquist plots were fitted using the EC-LAB software.

RESULTS AND DISCUSSION

Determining the crystal structures of chiral R-[QH]MS, achiral [QHco]MS, and the racemic [QHrac]MS salts was essential to understand the reasons behind their phase transition behaviors in increasing temperature and proton conduction features associated with the insurgence of plastic phases. Consequently, the crystal structures of these salts were specified from the data collected at room temperature. The structures of the achiral [QHco]MS and of the racemic [QHrac]MS compounds had to be determined from powder data since all attempts to grow single crystals were fruitless, and only polycrystalline samples could be obtained (see Supporting Information), while for R-[QH]MS, we were able to grow single-crystal specimens. For this latter species, correspondence between the structure determined from the single crystal and that of the polycrystalline sample was ascertained by successful comparison between the experimental powder pattern and that calculated based on the single-crystal structure. Among the series, only R-[QH]MS exhibited a chiral crystal structure, while the remaining salts had centrosymmetric crystal structures (see Table S1 for crystallographic details).

[QHco]MS crystallizes at room temperature in the orthorhombic space group Pnma (see Table S1 for details). As reported in Figure 1, the salt forms discrete anion/cation pairs interacting through a bifurcated charge-assisted hydrogen bond: N−H···O [2.932(9) Å], while the carbonyl group is engaged only in weak C−H···O bifurcated interactions with neighboring cations [3.429(1) Å]. At RT, the racemic salt, [QHrac]MS, crystallizes in the monoclinic space group $P2_1/c$ (see Table S1 for details), in which cations and anions form 1D charge-assisted hydrogen-bonded chains through cation−cation N−H···O 2.683(4) Å] and anion−cation O−H···O [2.660(3) Å] interactions running along the b-axis.

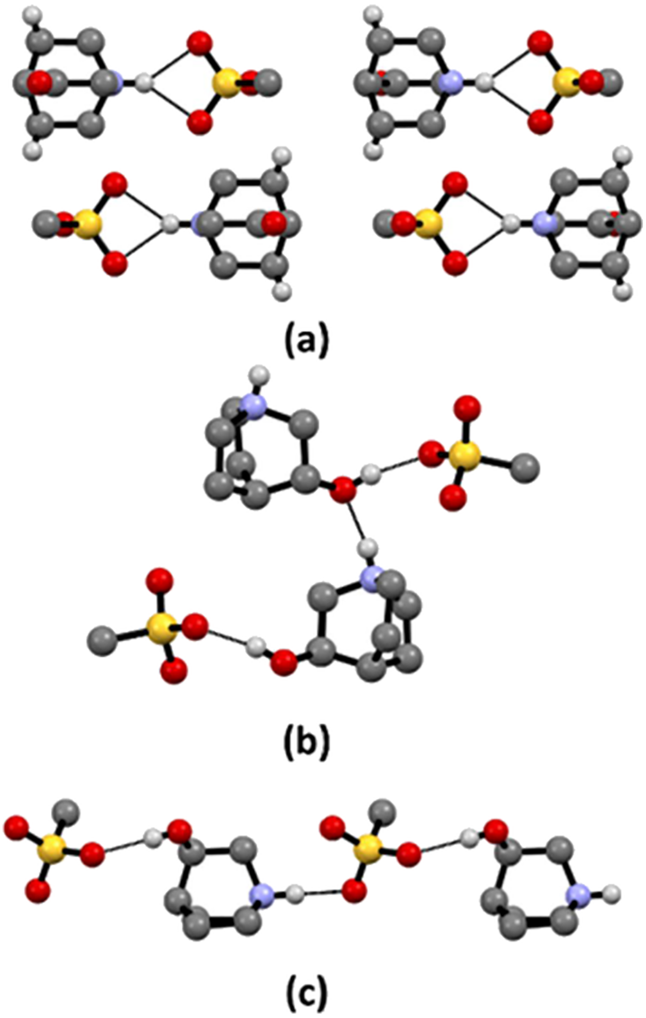

Figure 1. Representation of the intermolecular interactions detected within (a) the achiral [QHco]MS, (b) the racemic [QHrac]MS, and (c) the enantiopure R-[QH]MS. H_{CH} atoms are omitted for clarity.

The enantiopure compound R-[QH]MS crystallizes in the orthorhombic space group $P2_12_12_1$ (see Table S1 for details). Contrarywise, to its racemic analogue, within crystalline R-[QH]MS, the 1D charge-assisted hydrogen-bonded chains through N−H···O [2.786(4) Å] and O−H···O [2.744(4) Å] interactions along the b-axis direction arise from an alternation of cations and anions (Figure 1). Experimental powder XRD patterns, recorded at RT, match well with the simulated one from the single-crystal structure, revealing the high crystallinity and purity of the phase (see Supporting Information). For all compounds, the electrostatic compression[70,71] between oppositely charged ions combined with the strength and high directionality coming from the nature of hydrogen bonds leads to the formation of relatively shorter bonds in anion–cation interactions. Significant differences among the series are present at the level of the crystal packing, and as we shall see in the following, these differences will be responsible for the occurrence, or not, of the plastic phase transition.

Thermal analysis for [QHco]MS indicates stability up to ca. 130 °C (see Supporting Information), whereas DSC did not spot any transitions below the degradation temperature (investigated range: RT-130 °C), i.e., no plastic or melting transition was detected for this compound. On the other hand, [QHrac]MS has higher thermal stability with degradation onsetting at around 180 °C, while DSC displays an endothermic process at 150 °C with a ΔH of 21.8 kJ mol^{-1} and ΔS of 51.3 J mol^{-1} K^{-1}, which was assessed as melting from hot-stage microscopy (HSM) measurements (see Supporting Information). Finally, the enantiopure crystal R-[QH]MS shows the most interesting thermal behavior among the whole series of salts examined in this study. R-[QH]MS possesses a higher thermal stability up to ca. 230 °C (see TGA in the Supporting Information). At the same time, DSC indicates a reversible phase transition peaking at ca. 130 °C (heating cycle) with a ΔH of 20.7 kJ mol^{-1}, a ΔS of 51.10 J mol^{-1} K^{-1}, and with ca. 20 °C of hysteresis (see Supporting Information).

HSM and variable-temperature powder XRD experiments were performed to elucidate the nature of this process. In agreement with the DSC data, upon increasing the temperature, as shown in Figure 2a, R-[QH]MS single crystals undergo a solid–solid transition accompanied by a reversible birefringence loss and regain. At the same time, the powder XRD pattern recorded at 140 °C shows the disappearance of many diffraction peaks (Figure 2b). The smaller number of peaks observed reflects an increase in crystal symmetry, in fact, a cubic unit cell (a = 9.5 Å and V = 860 Å^3) was indexed, which agrees with other similar reported plastic crystals.[33,35,43,54] Plastic phases usually display a highly symmetrical crystal lattice with a salt-like structure and with no birefringence; i.e., cubic systems;[30,47,72,73] therefore, both experiments provide clear hints of plastic crystal formation.

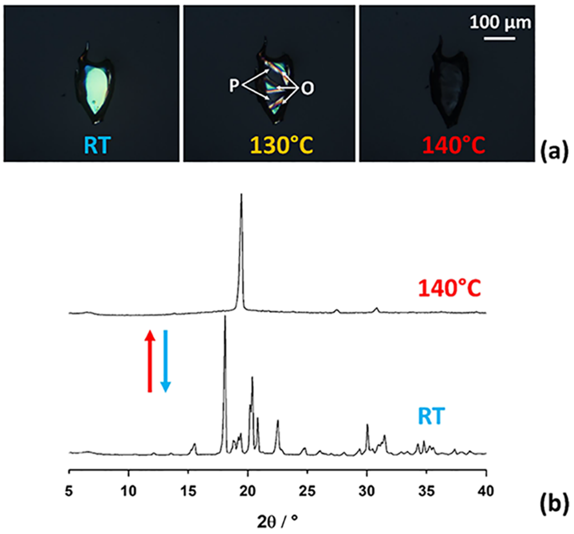

Figure 2. (a) Cross-polarized HSM pictures taken on a R-[QH]MS single crystal before, during, and after the solid–solid transition; P and O indicate the concomitant Plastic (P) and Ordered (O) domains detected across the phase transitions. (b) Powder XRD patterns recorded at RT and at high temperature (140 °C) for a polycrystalline sample of R-[QH]MS.

To prove our hypothesis about the nature of the solid–solid transition and gain further insights into the vibrational properties of the quinuclidinolium salts in their high-temperature phases, we measured the Raman spectra of the three systems as a function of the temperature. By focusing on the low-frequency range, i.e., below 150 cm^{-1}, we were able to probe the dynamics of the lattice, investigating the modes which represent the fingerprint of each specific crystal structure. The same strategy has been already successfully adopted in the study of plastic crystals in neutral[74] and ionic systems[33] as a function of temperature and pressure. The VT micro-Raman spectra of the R-[QH]MS system in the temperature interval of interest are reported in Figure 3. The number of the bands detected is a function of the characteristics and the symmetry of the crystal.[75−77] In detail, Figure 3a reports the evolution of the lattice phonon modes of the orthorhombic system, together with the intramolecular modes of lowest energy in the range of 150–380 cm^{-1}, thus allowing for the check of both the crystal and the molecular dynamics on the same spot and at the same temperature. The pattern of the lattice phonon vibrations gets abruptly washed away above 125 °C, i.e., above the transition temperature. This confirms the sudden occurrence of a high degree of molecular disorder in the system, while its long-range order is maintained, resulting in the averaged cubic structure detected by the X-ray measurements. A further evidence of local

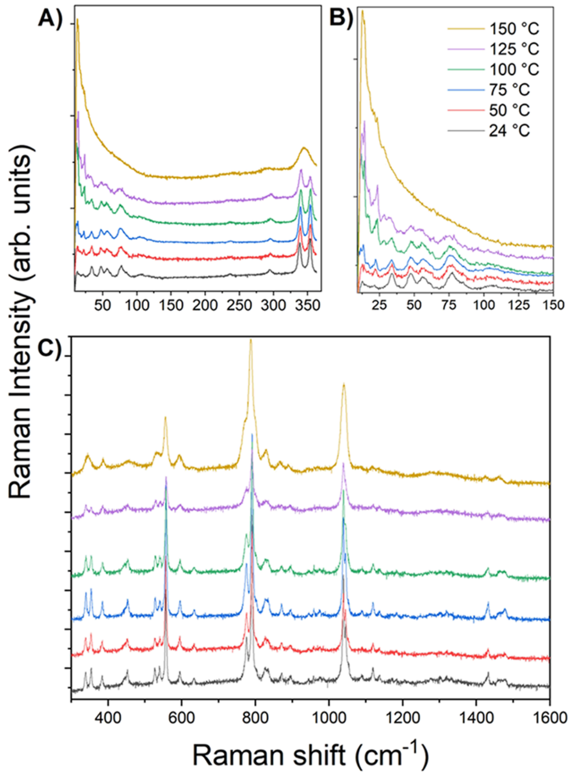

Figure 3. VT-Raman spectra of the R-[QH]MS system. (a) Wavenumber range comprising lattice phonons and low energy intramolecular vibrations; (b) zoom-in on the lattice phonon region, where crystal symmetry changes are detected; and (c) wavenumber range of all intramolecular vibrations.

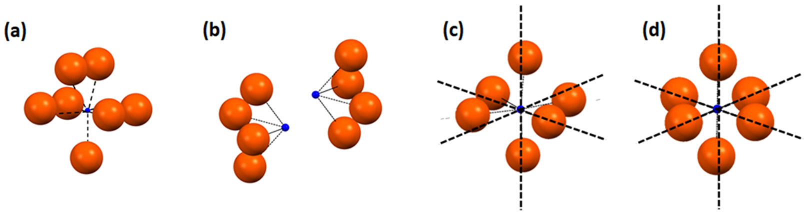

Figure 4. Comparison between the ionic environments of (a) [QHco]MS, (b) the racemic [QHrac]MS, (c) enantiopure R-[QH]MS with gridlines showing the differences between the "quasi-cubic" arrangement and an ideal octahedral arrangement, and (d) the salt-like cubic plastic phase simulated based on the high-temperature XRD pattern measurement. The cations and anions are depicted as blue and orange spheres, respectively.

disorder is given by the replacement at the transition of the lattice phonon pattern by a diffuse Rayleigh wing (RW) starting at around 100 cm^{-1} (see a zoom-in of lattice modes region in Figure 3b), a phenomenon already reported for adamantanes, which are the typical benchmark for plastic crystal spectroscopic features.[74] A somewhat similar behavior is observed for the two intramolecular modes peaked at 340 and 353 cm^{-1}, which are assigned to the crystal -SO_3^- asymmetric rocking by Parked and Zhong.[78] Such SO_3^- doublet is subjected to some minor broadening on increasing temperature, but keeps its character, suddenly merging into a single broad band only above the transition. This effect confirms that at the transition, the methanesulfonate gets disordered with symmetry breaking.

Figure 3c displays the system VT-Raman spectra over a wide wavenumber interval of intramolecular vibrations. As can be seen, the spectral features keep unchanged on increasing temperature, ruling out the occurrence of any chemical damage or degradation due to heating. Besides the already described SO_3^- asymmetric rocking vibrations, the assignment of several other peaks to either the cation $[QH]^+$ and anion MS^- supports this conclusion. For instance, the peak at 788 cm^{-1}, which dominates the spectrum, can be assigned to the C−N−C and C−C−C stretching modes[79] of the cation $[QH]^+$, while the near peak at 770 cm^{-1} and the one centered at 556 cm^{-1} correspond to the C−S stretching and $-SO_3^-$ symmetric bending, respectively, of the anion MS^-.[78,80] Finally, the intense band centered at 1040 cm^{-1} arises from the convolution of more vibrational modes assigned to both $[QH]^+$ symmetric and asymmetric stretching involving CCC and CNC groups, and -SO_3^- symmetric stretching.[78−80]

Over the entire spectral range, the plastic phase transition is highlighted by the sudden and simultaneous broadening of all the intramolecular modes of both $[QH]^+$ and MS^-, meaning that the two components of the crystalline system become orientationally disordered in a concerted way. In a previous investigation of IPCs, we did observe transitions to disordered phases separately for the cation and anion, with the formation of an intermediate semi-ordered phase spectroscopically identified by the presence of a boson peak in the low-frequency Raman spectrum.[33] VT micro-Raman spectra were also recorded for the achiral [QHco]MS and for the racemic [QHrac]MS compounds. As shown in Figure S9, no order−disorder plastic phase transition was detected for either system. In fact, the lattice phonon patterns are still recognizable up to 160 and 200 °C, respectively, while the doublet of the diagnostic intramolecular vibrational modes in the range 340−350 cm^{-1} does not merge and show broadening on increasing temperature. These results agree with the X-ray and thermal analysis and the electrochemical measurements presented below.

Despite the high degree of similarity of the components, only the enantiopure R-[QH]MS undergoes plastic transition; therefore, we wondered about the reasons for such diverse behaviors among the series. A possible rationalization comes from considering a plausible mechanism for plastic crystal formation in combination with the relative size of ions constituting the materials, and the ionic environment around each cation. In principle, during a plastic transition, as the temperature increases, the degrees of freedom of the fragments increase too, and librations and rotations begin. Weak and directional intermolecular interactions such as charge-assisted hydrogen bonds start fading at this stage until a plastic crystal phase is attained, mainly held, and stabilized by nondirectional Coulombic forces. Finally, ions must rearrange in the crystal lattice to minimize repulsion and maximize attractions; for example, ~~in~~the cubic systems exhibit salt-like structures with six anions around each cation and vice versa, which is typical of the plastic phases.[33,35,47,54] Based on the van der Waals radii of the ions, radii are 1.9 Å for the methanesulfonate and 2.9−3.1 Å for the cations, while their radius ratios ($\rho = r_{anion}/r_{cation}$) are 0.67−0.61; thus, according to the radius ratio rule in ionic crystals, a favorable arrangement can be found in an octahedral disposition (CN = 6).[47,81] Again, all of them fulfill the coordination conditions and could afford stable plastic phases upon application of temperature, but as anticipated above, significant differences are detected at the level of crystal packing (Figure S8) which mirrors in diverse ionic environments for each cation. Although ions possess high mobility within plastic phases, their components do not reach a degree of freedom as high as that of a liquid, allowing them to flow over the entire crystal. Therefore, low diffusion hinders a complete rearrangement to mimic the salt-like disposition of ions unless they are almost preorganized within the ordered phases. This is particularly evident if we consider the series of this study. For [QHco]MS and [QHrac]MS, with seven and four anions surrounding each cation, the ionic disposition is quite far from reaching an octahedral disposition (Figure 4), preventing, de facto, the ordered crystal from rearranging to a cubic phase upon temperature increase. In crystalline R-[QH]MS, on the contrary, the anions are almost perfectly aligned around the cation (Figure 4) allowing to attain, with minimal motion, a coordination number of six, corresponding to the plastic phase in a salt-like cubic system.

Finally, the proton conductivity of R-[QH]MS, [QHrac]MS, and [QHco]MS was investigated by EIS within their thermally stable ranges under anhydrous conditions. Pellets of the samples were placed between two stainless steel blocking electrodes housed in a two-electrode cell and tested in an Ar-filled glove box (see Supporting Information). Figure S10 reports the evolution of the Nyquist plots at increased temperatures, recorded for the different samples. The plots collected at the lowest and highest temperatures present a single semicircle with a low-frequency tail and were analyzed referring to the equivalent circuit reported in Figure S11. The equivalent circuit is composed by the electronic resistance of the cell ($R1$, from cables and blocking electrodes) that is in series with an ($R2Q2$) branch, where $R2$ is the bulk ionic resistance of the pellet in parallel with the constant phase element $Q2$. $Q2$ describes the double-layer capacitance at the two ionic conductor/electrode interfaces. It was used to represent the deviation from an ideal capacitive response that has been related to surface roughness.[82−84]

Figure 5 shows the R-[QH]MS Nyquist plots collected at 71 °C, where the phase is ordered, at 120 °C, corresponding to the phase transition, and at 137 °C, where R-[QH]MS is plastic. It is evident that the low-frequency semicircle dramatically shrinks moving from the ordered to the plastic state. Notably, in the transition regime, the formation of the second phase is bringing about a second semicircle in the Nyquist plots, located at the highest frequencies. The second semicircle (observed in the phase transition temperature range) was analyzed considering a second ($R3Q3$) branch added in series with the previous one ($R2Q2$).

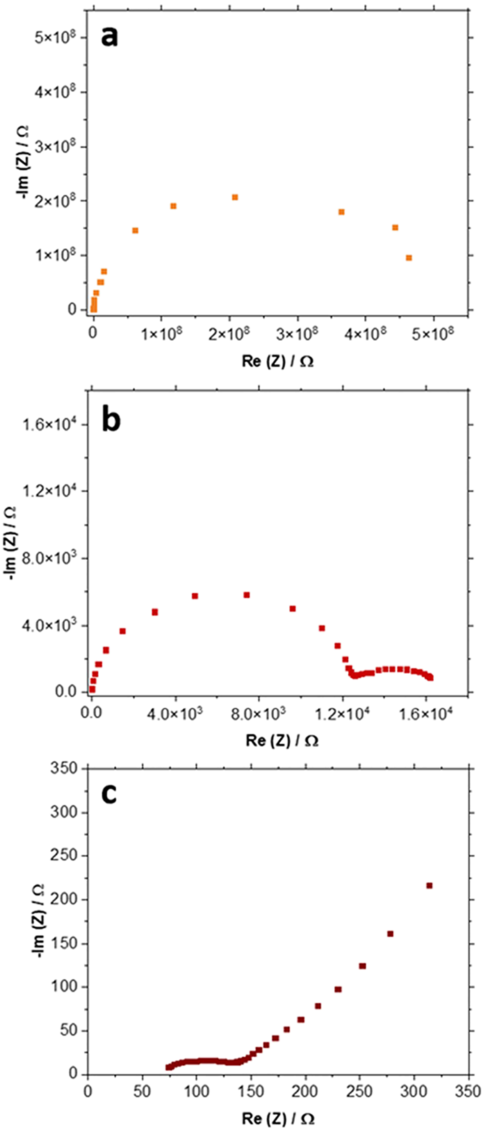

Figure 5. Comparison between the ionic environments of the enantiopure R-[QH]MS (left) and the salt-like cubic plastic phase simulated based on the high-temperature XRD pattern measurement (right). The cations and anions are depicted as blue and orange spheres, respectively.

Upon increasing temperature, this second semicircle gradually substitutes the first one that belongs to the ordered phase. Figure 6 reports the ionic conductivities (σ) calculated from the electrolyte resistance (R) that in turn was determined from the diameter of the Nyquist plot high-frequency semicircle ($R2$). In the case of the spectra collected in the transition region, we used the total resistance evaluated as the sum of the diameters of the two semicircles ($R2$ + $R3$).

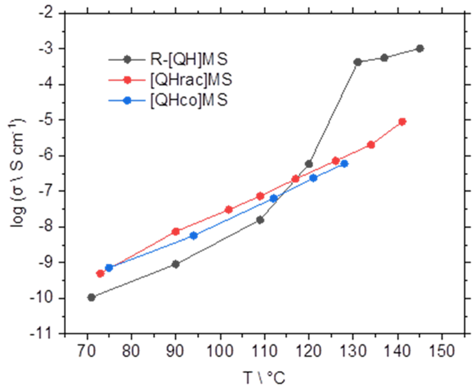

Figure 6. Trend of the ionic conductivity of R-[QH]MS, [QHrac]-MS, and [QHco]MS vs temperature.

Specifically, σ was calculated according to the following equation:

$$\rho = \frac{1}{\sigma} = \frac{A \cdot R}{L}$$

where ρ is the resistivity, A is the pellet cross-sectional area, and L is the pellet thickness.

The ionic conductivity of R-[QH]MS at RT was found to be lower than 10^{-11} S cm^{-1} which increased to 1.57×10^{-8} S cm^{-1} with increasing temperature up to 109 °C, i.e., right before the onset of the plastic phase. Unlike the other two compounds, a drastic increase is observed in the conductivity of R-[QH]MS owing to the plastic phase transition. Indeed, σ reached 4.25×10^{-4} S cm^{-1} at 131 °C. The gradual phase transition behavior of enantiopure R-[QH]MS was also observed at the HSM (see Figure 2a). The highest conductivity of 1.03×10^{-3} S cm^{-1} was reached at 145 °C which is considered a high value under anhydrous conditions at this temperature range as a pure material.[17,20,85,86] The Arrhenius plots of three heating and cooling cycles of R-[QH]MS (see Figure S12) compared with those of [QHrac]-MS, and [QHco]MS (see Figure S13) are drawn not only to show reproducibility but also to calculate the activation energies before and after the phase transition regions by using the Arrhenius equation:

$$\sigma(T) = \frac{\sigma_0}{T}\exp\left(-\frac{E_a}{k_b \cdot T}\right)$$

where σ_0 is a preexponential constant and E_a is the activation energy, k_b is the Boltzmann constant, and T is the temperature. The E_a values of [QHrac]MS, [QHco]MS, and ordered phase of R-[QH]MS are found to be 151, 143, and 146 kJ mol^{-1}, respectively. As a typical behavior of OIPCs, after the plastic phase transition, the E_a is decreased to 92 kJ mol^{-1}, indicating point defect-mediated conduction through bulk plastic phase in the case of enantiopure R-[QH]MS.[60,61,87]

CONCLUSIONS

In conclusion, we have investigated the plastic phase transition features of a series of methanesulfonate salts with various globular cations, including the achiral [QHco]$^+$, the racemic [QHrac]$^+$, and the enantiopure R-[QH]$^+$.

Despite being quite similar in terms of shapes and volumes, the different symmetry of each cation profoundly affects the intermolecular interaction patterns and, thus, crystal packings; consequently, the salts [QHco]MS, [QHrac]MS, and R-[QH]MS are not isostructural and display a variety of arrangements of the ions, which are reflected by the different phase transition behaviors.

Interestingly, only the enantiopure salt R-[QH]MS exhibited plastic phase behavior with temperature, which was confirmed by XRD, thermal, and micro-Raman spectroscopy measurements, whereas [QHco]MS and [QHrac]MS underwent melting as the temperature was increased; the R-[QH]MS salt was also found to be an excellent proton-conducting material at high temperature with ionic conductivity passing from 10^{-11} S cm^{-1} (RT) to 1.57×10^{-8} S cm^{-1} (109 °C) and increasing nonlinearly to 1.03×10^{-3} S cm^{-1} at around 145 °C which is attributed to a marked acceleration of motion associated with temperature variations and the plastic phase transition.

These findings point out that the R-[QH]MS salt is potentially a good candidate as a dopant agent to be used in Nafion-based membranes to compensate the loss of proton conductivity because of the dehydration above 80 °C, and work is already ongoing. Furthermore, our findings could enlarge the design strategies of novel solid-state electrolytes based on plastic crystals by considering the packing features besides the already established shape and size factors of the components.

ASSOCIATED CONTENT

Supporting Information

The Supporting Information is available free of charge at https://pubs.acs.org/doi/10.1021/acs.cgd.3c00145.

> Additional information concerning PXRD, Rietveld refinement plots, TGA, and DSC traces, VT-Raman, EIS, and Arrhenius plots and X-ray crystallographic data for [QHco]MS, [QHrac]MS, and R-[QH]MS (PDF)

Accession Codes

CCDC 2235832−2235834 contain the supplementary crystallographic data for this paper. These data can be obtained free of charge via www.ccdc.cam.ac.uk/data_request/cif, or by emailing data_request@ccdc.cam.ac.uk, or by contacting The Cambridge Crystallographic Data Centre, 12 Union Road, Cambridge CB2 1EZ, UK; fax: +44 1223 336033.

AUTHOR INFORMATION

Corresponding Authors

Tommaso Salzillo − *Department of Industrial Chemistry "Toso Montanari" Alma Mater Studiorum, University of Bologna, 40124 Bologna, Italy; Department of Chemical and Biological Physics, Weizmann Institute of Science, Rehovot 76100, Israel;* orcid.org/0000-0002-9737-2809; Email: tommaso.salzillo@unibo.it

Francesca Soavi − *Department of Chemistry "Giacomo Ciamician" Alma Mater Studiorum, University of Bologna, 40126 Bologna, Italy;* orcid.org/0000-0003-3415-6938; Email: fracesca.soavi@unibo.it

Simone d'Agostino − *Department of Chemistry "Giacomo Ciamician" Alma Mater Studiorum, University of Bologna, 40126 Bologna, Italy;* orcid.org/0000-0003-3065-5860; Email: simone.dagostino2@unibo.it

Authors

Samet Ocak − *Department of Chemistry "Giacomo Ciamician" Alma Mater Studiorum, University of Bologna, 40126 Bologna, Italy*

Federico Poli − *Department of Chemistry "Giacomo Ciamician" Alma Mater Studiorum, University of Bologna, 40126 Bologna, Italy;* orcid.org/0000-0001-9891-2785

Dario Braga − *Department of Chemistry "Giacomo Ciamician" Alma Mater Studiorum, University of Bologna, 40126 Bologna, Italy;* orcid.org/0000-0003-4162-4779

Fabrizio Tarterini − *Department of Industrial Chemistry "Toso Montanari" Alma Mater Studiorum, University of Bologna, 40124 Bologna, Italy*

Gianluca Carì − *Department of Chemistry "Giacomo Ciamician" Alma Mater Studiorum, University of Bologna, 40126 Bologna, Italy*

Elisabetta Venuti − *Department of Industrial Chemistry "Toso Montanari" Alma Mater Studiorum, University of Bologna, 40124 Bologna, Italy;* orcid.org/0000-0003-3493-7953

Complete contact information is available at: https://pubs.acs.org/10.1021/acs.cgd.3c00145

Author Contributions

The manuscript was written through contributions of all authors. All authors have given approval to the final version of the manuscript. S.O. and F.P. contributed equally.

Notes

The authors declare no competing financial interest.

ACKNOWLEDGMENTS

All the authors acknowledge University of Bologna for financial support (RFO-scheme). S.D., F.P., and F.S. thank the Italian MUR (Fondi PNRR-CNMS-Spoke 13-MOST Code: CN00000023) for financial support. T.S. thanks the "Programma per Giovani Ricercatori - Rita Levi Montalcini - year 2020 of the Italian Ministry of University and Research (MUR) for the financial support. Project funded under the National Recovery and Resilience Plan (PNRR), Mission 04 Component 2 Investment 1.5 − Next Generation EU, call for tender n. 3277 dated 30/12/2021 (Award Number: 0001052 dated 23/06/2022).

REFERENCES

(1) Liu, X.; Guo, B.; Zhang, L.; Zhao, S.; Dong, Y.; Zhao, Z. Construction of a Unique 2-D Layered Vanadoborate with Water-Assisted Proton Conductivity. *New J. Chem.* **2022**, *46*, 16352−16358.

(2) Bakangura, E.; Wu, L.; Ge, L.; Yang, Z.; Xu, T. Mixed Matrix Proton Exchange Membranes for Fuel Cells: State of the Art and Perspectives. *Prog. Polym. Sci.* **2016**, *57*, 103−152.

(3) Ahmad Fauzi, A. S.; Hamidah, N. L.; Sato, S.; Shintani, M.; Putri, G. K.; Kitamura, S.; Hatakeyama, K.; Quitain, A. T.; Kida, T. Carbon-Based Potentiometric Hydrogen Sensor Using a Proton Conducting

Graphene Oxide Membrane Coupled with a WO3 Sensing Electrode. *Sens. Actuators B Chem.* **2020**, *323*, No. 128678.

(4) Tahir, N. N. M.; Baharuddin, N. A.; Samat, A. A.; Osman, N.; Somalu, M. R. A Review on Cathode Materials for Conventional and Proton-Conducting Solid Oxide Fuel Cells. *J. Alloys Compd.* **2022**, *894*, No. 162458.

(5) Łatoszyńska, A. A.; Taberna, P. L.; Simon, P.; Wieczorek, W. Proton Conducting Gel Polymer Electrolytes for Supercapacitor Applications. *Electrochim. Acta* **2017**, *242*, 31−37.

(6) Thiam, B. G.; Vaudreuil, S. Review—Recent Membranes for Vanadium Redox Flow Batteries. *J. Electrochem. Soc.* **2021**, *168*, No. 070553.

(7) Kusoglu, A.; Weber, A. Z. New Insights into Perfluorinated Sulfonic-Acid Ionomers. *Chem. Rev.* **2017**, *117*, 987−1104.

(8) Yang, X.; Zhu, H.; Jiang, F.; Zhou, X. Notably Enhanced Proton Conductivity by Thermally-Induced Phase-Separation Transition of Nafion/Poly(Vinylidene Fluoride) Blend Membranes. *J. Power Sources* **2020**, *473*, No. 228586.

(9) Patel, H. A.; Mansor, N.; Gadipelli, S.; Brett, D. J. L.; Guo, Z. Superacidity in Nafion/MOF Hybrid Membranes Retains Water at Low Humidity to Enhance Proton Conduction for Fuel Cells. *ACS Appl. Mater. Interfaces* **2016**, *8*, 30687−30691.

(10) Rautenberg, M.; Bhattacharya, B.; Das, C.; Emmerling, F. Mechanochemical Synthesis of Phosphonate-Based Proton Conducting Metal-Organic Frameworks. *Inorg. Chem.* **2022**, *61*, 10801−10809.

(11) Mauritz, K. A.; Moore, R. B. State of Understanding of Nafion. *Chem. Rev.* **2004**, *104*, 4535−4586.

(12) Moilanen, D. E.; Spry, D. B.; Fayer, M. D. Water Dynamics and Proton Transfer in Nafion Fuel Cell Membranes. *Langmuir* **2008**, *24*, 3690−3698.

(13) Luo, J.; Conrad, O.; Vankelecom, I. F. J. Imidazolium Methanesulfonate as a High Temperature Proton Conductor. *J. Mater. Chem. A Mater.* **2013**, *1*, 2238−2247.

(14) D'Epifanio, A.; Mecheri, B.; Fabbri, E.; Rainer, A.; Traversa, E.; Licoccia, S. Composite Ormosil/Nafion Membranes as Electrolytes for Direct Methanol Fuel Cells. *J. Electrochem. Soc.* **2007**, *154*, B1148.

(15) Rana, U. A.; Vijayaraghavan, R.; Doherty, C. M.; Chandra, A.; Efthimiadis, J.; Hill, A. J.; MacFarlane, D. R.; Forsyth, M. Role of Defects in the High Ionic Conductivity of Choline Triflate Plastic Crystal and Its Acid-Containing Compositions. *J. Phys. Chem. C* **2013**, *117*, 5532−5543.

(16) Qian, Y.; Zhang, J.; Wang, Y. M.; Yao, W. W.; Shao, D. S.; Ren, X. M. Magnetic Bistable Organic Ionic Plastic Crystal with Room Temperature Ion Conductivity Comparable to NASICON and Superionic Conduction in a Broad Temperature Window†. *Mater. Chem. Front.* **2022**, *6*, 793−801.

(17) Zhu, H.; MacFarlane, D. R.; Pringle, J. M.; Forsyth, M. Organic Ionic Plastic Crystals as Solid-State Electrolytes. *Trends Chem.* **2019**, *1*, 126−140.

(18) Pringle, J. M.; Howlett, P. C.; MacFarlane, D. R.; Forsyth, M. Organic Ionic Plastic Crystals: Recent Advances. *J. Mater. Chem.* **2010**, *20*, 2056−2062.

(19) Das, S.; Mondal, A.; Reddy, C. M. Harnessing Molecular Rotations in Plastic Crystals: A Holistic View for Crystal Engineering of Adaptive Soft Materials. *Chem. Soc. Rev. R. Soc. Chem.* **2020**, *49*, 8878−8896.

(20) Horike, S.; Umeyama, D.; Inukai, M.; Itakura, T.; Kitagawa, S. Coordination-Network-Based Ionic Plastic Crystal for Anhydrous Proton Conductivity. *J. Am. Chem. Soc.* **2012**, *134*, 7612−7615.

(21) Pas, S. J.; Huang, J.; Forsyth, M.; MacFarlane, D. R.; Hill, A. J. Defect-Assisted Conductivity in Organic Ionic Plastic Crystals. *J. Chem. Phys.* **2005**, *122*, No. 064704.

(22) Qian, Y.; Shao, D. S.; Yao, W. W.; Wan, N.; Wang, X. Z.; Ren, X. M. Ion Conduction and Complicated Phase Transition Behaviors in an Organic Ion Plastic Crystal, [Tetra-n-Butylammonium]2[Ni-(Maleonitriledithiolate)2]. *J. Phys. Chem. C* **2020**, *124*, 20722−20729.

(23) Qian, Y.; Shao, D. S.; Yao, W. W.; Yao, Z. Y.; Wang, L.; Liu, W. L.; Ren, X. M. A Promising Phase Change Material with Record High Ionic Conductivity over a Wide Temperature Range of a Plastic Crystal Phase and Magnetic Thermal Memory Effect. *ACS Appl. Mater. Interfaces* **2020**, *12*, 28129−28138.

(24) Yang, K.; Zhang, Z.; Liao, Z.; Yang, L.; Hirano, S. I. Organic Ionic Plastic Crystal-Polymer Solid Electrolytes with High Ionic Conductivity and Mechanical Ability for Solid-State Lithium Ion Batteries. *ChemistrySelect* **2018**, *3*, 12595−12599.

(25) Zhou, H.; Xie, J.; Bao, L.; Qiao, S.; Sui, J.; Wang, J. Poly(Carbonate)-Based Ionic Plastic Crystal Fast Ion-Conductor for Solid-State Rechargeable Lithium Batteries. *J. Energy Chem.* **2022**, *73*, 360−369.

(26) Karlen, S. D.; Garcia-Garibay, M. A. Amphidynamic Crystals: Structural Blueprints for Molecular Machines. In *Molecular Machines*, Kelly, T. R., Eds.; Topics in Current Chemistry; Springer: Berlin, Heidelberg, 2005; vol. *262*, pp. 179 −227.

(27) Naumov, P.; Karothu, D. P.; Ahmed, E.; Catalano, L.; Commins, P.; Mahmoud Halabi, J.; Al-Handawi, M. B.; Li, L. The Rise of the Dynamic Crystals. *J. Am. Chem. Soc.* **2020**, *142*, 13256−13272.

(28) D'Agostino, S.; Fornasari, L.; Grepioni, F.; Braga, D.; Rossi, F.; Chierotti, M. R.; Gobetto, R. Precessional Motion in Crystalline Solid Solutions of Ionic Rotors. *Chem. − Eur. J.* **2018**, *24*, 15059−15066.

(29) García, Y.; O'Dell, L. A. Understanding the Interfacial Region in Organic Ionic Plastic Crystal Composite Electrolyte Materials by Solid-State NMR. *Curr. Opin. Colloid Interface Sci.* **2022**, *61*, No. 101632.

(30) Timmermans, J. Plastic Crystals: A Historical Overview. *J. Phys. Chem. Solids* **1961**, *18*, 1−8.

(31) Seddon, K. R. A Taste of the Future. *Nat. Mater.* **2003**, *2*, 363.

(32) Perry, D.; Page, A.; Chen, B.; Frenguelli, B. G.; Unwin, P. R. Differential-Concentration Scanning Ion Conductance Microscopy. *Anal. Chem.* **2017**, *89*, 12458−12465.

(33) Ocak, S.; Birolo, R.; Carì, G.; Bordignon, S.; Chierotti, M. R.; Braga, D.; Gobetto, R.; Salzillo, T.; Venuti, E.; Yaffe, O.; d'Agostino, S. Engineering Plastic Phase Transitions via Solid Solutions: The Case of "Reordering Frustration" in Ionic Plastic Crystals of Hydroxyquinuclidinium Salts. *Mol. Syst. Des. Eng.* **2022**, *7*, 950−962.

(34) Fornasari, L.; Olejniczak, A.; Rossi, F.; d'Agostino, S.; Chierotti, M. R.; Gobetto, R.; Katrusiak, A.; Braga, D. Solid-State Dynamics and High-Pressure Studies of a Supramolecular Spiral Gear. *Chem. − Eur. J.* **2020**, *26*, 5061−5069.

(35) D'Agostino, S.; Fornasari, L.; Braga, D. Binary and Ternary Solid Solutions of Ionic Plastic Crystals, and Modulation of Plastic Phase Transitions. *Cryst. Growth Des.* **2019**, *19*, 6266−6273.

(36) Warrington, A.; Kang, C. S. M.; Forsyth, C.; Doherty, C. M.; Acharya, D.; O'Dell, L. A.; Sirigiri, N.; Boyle, J. W.; Hutt, O. E.; Forsyth, M.; Pringle, J. M. Thermal, Structural and Dynamic Properties of Ionic Liquids and Organic Ionic Plastic Crystals with a Small Ether-Functionalised Cation. *Mater. Chem. Front.* **2022**, *6*, 1437−1455.

(37) Casimiro, A.; Lugger, J.; Lub, J.; Nijmeijer, K. Non-Globular Organic Ionic Plastic Crystal Containing a Crown-Ether Moiety − Tuning Its Behaviour Using Sodium Salts. *ChemPhysChem* **2022**, *23*, No. e202200258.

(38) Sirigiri, N.; Chen, F.; Forsyth, C. M.; Yunis, R.; O'Dell, L.; Pringle, J. M.; Forsyth, M. Factors Controlling the Physical Properties of an Organic Ionic Plastic Crystal. *Mater. Today Phys.* **2022**, *22*, No. 100603.

(39) Pogorzelec-Glaser, K.; Rachocki, A.; Ławniczak, P.; Łapiński, A.; Tritt-Goc, J. Synthesis and Characterization of a New Proton-Conducting Material Based on Imidazole and Selenic Acid. *Solid State Ionics* **2012**, *227*, 96−101.

(40) Ggor, A.; Piecha, A.; Jakubas, R.; Miniewicz, A. Crystal Structure and Characterization of a Novel Acentric Imidazolium Analog [C3N2H5+][Br-]. *Chem. Phys. Lett.* **2011**, *503*, 134−138.

(41) Yang, C. K.; Chen, W. N.; Ding, Y. T.; Wang, J.; Rao, Y.; Liao, W. Q.; Xie, Y.; Zou, W.; Xiong, R. G. Directional Intermolecular Interactions for Precise Molecular Design of a High- T c Multiaxial Molecular Ferroelectric. *J. Am. Chem. Soc.* **2019**, *141*, 1781−1787.

(42) Braga, D.; Cojazzi, G.; Paolucci, D.; Grepioni, F. A Remarkable Water-Soluble (Molecular) Alloy with Two Tuneable Solid-to-Solid Phase Transitions. *Chem. Commun.* **2001**, 803−804.

(43) Li, P. F.; Tang, Y. Y.; Wang, Z. X.; Ye, H. Y.; You, Y. M.; Xiong, R. G. Anomalously Rotary Polarization Discovered in Homochiral Organic Ferroelectrics. *Nat. Commun.* **2016**, *7*, 13635.

(44) Sherwood, J. N. *The Plastically Crystalline State: Orientationally Disordered Crystals*; John Wiley & Sons, Cop., 1979.

(45) Park, C. B.; Sung, B. J. Heterogeneous Rotational Dynamics of Imidazolium-Based Organic Ionic Plastic Crystals. *J. Phys. Chem. B* **2020**, *124*, 6894−6904.

(46) Park, C. B.; Sung, B. J. Effects of Alkali Ion Dopants on the Transport Mechanisms and the Thermal Stabilities of Imidazolium-Based Organic Ionic Plastic Crystals. *Phys. Chem. Chem. Phys.* **2022**, *24*, 25171.

(47) Mochida, T.; Ishida, M.; Tominaga, T.; Takahashi, K.; Sakurai, T.; Ohta, H. Paramagnetic Ionic Plastic Crystals Containing the Octamethylferrocenium Cation: Counteranion Dependence of Phase Transitions and Crystal Structures. *Phys. Chem. Chem. Phys.* **2018**, *20*, 3019−3028.

(48) Kimata, H.; Sakurai, T.; Ohta, H.; Mochida, T. Phase Transitions, Crystal Structures, and Magnetic Properties of Ferrocenium Ionic Plastic Crystals with CF3BF3 and Other Anions. *ChemistrySelect* **2019**, *4*, 1410−1415.

(49) Lan, X.; Wang, X.; Zhang, D. X.; Mu, T.; Lan, X. Z. Cation and Anion Transfer in Quinuclidinium Hexafluorophosphate Plastic Crystal: Role of Constituent Ions and the Crystalline Structure. *J. Phys. Chem. C* **2021**, *125*, 21169−21178.

(50) Ai, Y.; Li, P. F.; Yang, M. J.; Xu, Y. Q.; Li, M. Z.; Xiong, R. G. An Organic Plastic Ferroelectric with High Curie Point. *Chem. Sci.* **2022**, *13*, 748−753.

(51) Lusi, M. A Rough Guide to Molecular Solid Solutions: Design, Synthesis and Characterization of Mixed Crystals. *CrystEngComm* **2018**, *20*, 7042−7052.

(52) Lusi, M. Engineering Crystal Properties through Solid Solutions. *Cryst. Growth Des.* **2018**, *18*, 3704−3712.

(53) Schur, E.; Nauha, E.; Lusi, M.; Bernstein, J. Kitaigorodsky Revisited: Polymorphism and Mixed Crystals of Acridine/Phenazine. *Chem. − Eur. J.* **2015**, *21*, 1735−1742.

(54) Matsumoto, K.; Nonaka, R.; Wang, Y.; Veryasov, G.; Hagiwara, R. Formation of a Solid Solution between [N(C2H5)4][BF4] and [N(C2H5)4][PF6] in Crystal and Plastic Crystal Phases. *Phys. Chem. Chem. Phys.* **2017**, *19*, 2053−2059.

(55) Gesi, K. Phase Diagram of N(CH3)4Mn1-XCuxCl3. *J. Phys. Soc. Jpn.* **1993**, *62*, 3805.

(56) Aston, J. G. Molecular Freedom in Solid Solutions of Hydrocarbons: Some Observations on Possible Causes Ofd Self-Diffusion. *Pure Appl. Chem.* **1961**, *2*, 231−240.

(57) D'Agostino, S.; Braga, D.; Grepioni, F.; Taddei, P. Intriguing Case of Pseudo-Isomorphism between Chiral and Racemic Crystals of Rac- and (S)/(R)2-(1,8-Naphthalimido)-2-Quinuclidin-3-Yl, and Their Reactivity toward I2and IBr. *Cryst. Growth Des.* **2014**, *14*, 821−829.

(58) Rekis, T.; D'Agostino, S.; Braga, D.; Grepioni, F. Designing Solid Solutions of Enantiomers: Lack of Enantioselectivity of Chiral Naphthalimide Derivatives in the Solid State. *Cryst. Growth Des.* **2017**, *17*, 6477−6485.

(59) Fecher, G. H.; Kübler, J.; Felser, C. Chirality in the Solid State: Chiral Crystal Structures in Chiral and Achiral Space Groups. *Materials* **2022**, *15*, 5812.

(60) Hori, Y.; Dekura, S.; Sunairi, Y.; Ida, T.; Mizuno, M.; Mori, H.; Shigeta, Y. Proton Conduction Mechanism for Anhydrous Imidazolium Hydrogen Succinate Based on Local Structures and Molecular Dynamics. *J. Phys. Chem. Lett.* **2021**, *12*, 5390−5394.

(61) Zhang, B.; Huang, Y.; Luo, J.; Li, A.; Yan, T. Local Proton Hopping Mechanism in Imidazolium-Based Plastic Crystal: An Ab Initio Molecular Dynamics Study. *Commun. Theor. Phys.* **2022**, *74*, No. 045502.

(62) Sheldrick, G. M. SHELXT - Integrated Space-Group and Crystal-Structure Determination. *Acta Crystallogr. A* **2015**, *71*, 3−8.

(63) Sheldrick, G. M. Crystal Structure Refinement with SHELXL. *Acta Crystallogr. C Struct. Chem.* **2015**, *71*, 3−8.

(64) Dolomanov, O. V.; Bourhis, L. J.; Gildea, R. J.; Howard, J. A. K.; Puschmann, H. OLEX2: A Complete Structure Solution, Refinement and Analysis Program. *J. Appl. Crystallogr.* **2009**, *42*, 339−341.

(65) Thorn, A.; Dittrich, B.; Sheldrick, G. M. Enhanced Rigid-Bond Restraints. *Acta Crystallogr. A* **2012**, *68*, 448−451.

(66) Macrae, C. F.; Bruno, I. J.; Chisholm, J. A.; Edgington, P. R.; McCabe, P.; Pidcock, E.; Rodriguez-Monge, L.; Taylor, R.; van de Streek, J.; Wood, P. A. Mercury CSD 2.0 - New Features for the Visualization and Investigation of Crystal Structures. *J. Appl. Crystallogr.* **2008**, *41*, 466−470.

(67) Altomare, A.; Cuocci, C.; Giacovazzo, C.; Moliterni, A.; Rizzi, R.; Corriero, N.; Falcicchio, A. EXPO2013: A Kit of Tools for Phasing Crystal Structures from Powder Data. *J. Appl. Crystallogr.* **2013**, *46*, 1231−1235.

(68) Altomare, A.; Giacovazzo, C.; Guagliardi, A. New techniques for indexing: N-TREOR. *J. Appl. Crystallogr.* **2000**, *33*, 1180−1186.

(69) Groom, C. R.; Bruno, I. J.; Lightfoot, M. P.; Ward, S. C. The Cambridge Structural Database. *Acta Crystallogr. B Struct. Sci. Cryst. Eng. Mater.* **2016**, *72*, 171−179.

(70) Dunitz, J. D.; Gavezzotti, A.; Rizzato, S. "coulombic Compression", a Pervasive Force in Ionic Solids. A Study of Anion Stacking in Croconate Salts. *Cryst. Growth Des.* **2014**, *14*, 357−366.

(71) Braga, D.; Bazzi, C.; Grepioni, F.; Novoa, J. J. Electrostatic Compression on Non-Covalent Interactions: The Case of π Stacks Involving Ions. *New J. Chem.* **1999**, *23*, 577−579.

(72) Brand, R.; Lunkenheimer, P.; Loidl, A. Relaxation Dynamics in Plastic Crystals. *J. Chem. Phys.* **2002**, *116*, 10386−10401.

(73) Webb, R. J.; Lowery, M. D.; Shiomi, Y.; Sorai, M.; Wittebort, R. J.; Hendrickson, D. N. Ferrocenium Hexafluorophosphate: Molecular Dynamics in the Solid State. *Inorg. Chem.* **1992**, *31*, 5211.

(74) Salzillo, T.; Girlando, A.; Brillante, A. Revisiting the Disorder-Order Transition in 1-X-Adamantane Plastic Crystals: Rayleigh Wing, Boson Peak, and Lattice Phonons. *J. Phys. Chem. C* **2021**, *125*, 7384−7391.

(75) Salzillo, T.; Rivalta, A.; Castagnetti, N.; D'Agostino, S.; Masino, M.; Grepioni, F.; Venuti, E.; Brillante, A.; Girlando, A. Spectroscopic Identification of Quinacridone Polymorphs for Organic Electronics. *CrystEngComm* **2019**, *21*, 3702−3708.

(76) Salzillo, T.; Venuti, E.; Femoni, C.; della Valle, R. G.; Tarroni, R.; Brillante, A. Crystal Structure of the 9-Anthracene-Carboxylic Acid Photochemical Dimer and Its Solvates by X-Ray Diffraction and Raman Microscopy. *Cryst. Growth Des.* **2017**, *17*, 3361−3370.

(77) Schrode, B.; Jones, A. O. F.; Resel, R.; Bedoya, N.; Schennach, R.; Geerts, Y. H.; Ruzié, C.; Sferrazza, M.; Brillante, A.; Salzillo, T.; Venuti, E. Substrate-Induced Phase of a Benzothiophene Derivative Detected by Mid-Infrared and Lattice Phonon Raman Spectroscopy. *ChemPhysChem* **2018**, *19*, 993−1000.

(78) Parker, S. F.; Zhong, L. Vibrational Spectroscopy of Metal Methanesulfonates: M = Na, Cs, Cu, Ag, Cd. *R Soc. Open Sci.* **2018**, *5*, No. 171574.

(79) Wojcik, N. A.; Kowalska, D. A.; Trzebiatowska, M.; Jach, E.; Ostrowski, A.; Bednarski, W.; Gusowski, M.; Staniorowski, P.; Cizman, A. Tunable Dielectric Switching of (Quinuclidinium)-[MnCl4] Hybrid Compounds. *J. Phys. Chem. C* **2021**, *125*, 16810−16818.

(80) Clarke, J. H. R.; Woodward, L. A. Raman Spectrophotometric Studies of the Dissociation of Methylmercuric Salts in Concentrated Aqueous Solution Part 2.-Djssociations of Methylmercuric Methanesulphonate and Methylmercuric Sulphate. *Trans. Faraday Soc.* **1966**, *62*, 3022.

(81) Atkins, P.; Overton, T.; Rourke, J.; Weller, M.; Armstrong, F.; Hagerman, M. *Shriver & Atkins' Inorganic Chemistry*, 5th Edition; WH Freeman and Company, 2006.

https://doi.org/10.1021/acs.cgd.3c00145

(82) Boukamp, B. A. Electrochemical Impedance Spectroscopy in Solid State Ionics: Recent Advances. *Solid State Ionics* **2004**, *169*, 65−73.

(83) Vadhva, P.; Hu, J.; Johnson, M. J.; Stocker, R.; Braglia, M.; Brett, D. J. L.; Rettie, A. J. E. Electrochemical Impedance Spectroscopy for All-Solid-State Batteries: Theory, Methods and Future Outlook. *ChemElectroChem* **2021**, *8*, 1930−1947.

(84) Careem, M. A.; Noor, I. S. M.; Arof, A. K. Impedance Spectroscopy in Polymer Electrolyte Characterization. In *Polymer Electrolytes: Characterization Techniques and Energy Applications*; Wiley: 2019; pp. 23−64.

(85) Dekura, S.; Mizuno, M.; Mori, H. Isotropic Anhydrous Superprotonic Conductivity Cooperated with Installed Imidazolium Molecular Motions in a 3D Hydrogen-Bonded Phosphate Network. *Angew. Chem. Int. Ed.* **2022**, *61*, No. e202212872.

(86) Li, X. M.; Dong, L. Z.; Liu, J.; Ji, W. X.; Li, S. L.; Lan, Y. Q. Intermediate-Temperature Anhydrous High Proton Conductivity Triggered by Dynamic Molecular Migration in Trinuclear Cluster Lattice. *Chem* **2020**, *6*, 2272−2282.

(87) Shekibi, Y.; Gray-Weale, A.; MacFarlane, D. R.; Hill, A. J.; Forsyth, M. Nanoparticle Enhanced Conductivity in Organic Ionic Plastic Crystals: Space Charge versus Strain Induced Defect Mechanism. *J. Phys. Chem. C* **2007**, *111*, 11463−11468.

(88) Braga, D.; Grepioni, F.; Maini, L.; d'Agostino, S. From solid state structure and dynamics to crystal engineering. *Eur. J. Chem.* **2018**, *2018*, 3597−3605.

(89) Desiraju, G. R. Crystal Engineering: From Molecule to Crystal. *J. Am. Chem. Soc.* **2013**, *135*, 9952−9967.